PAPER

Atomically dispersed asymmetric Cu–B pair on 2D carbon nitride synergistically boosts the conversion of CO into C_2 products†

Tianwei He,[a] Karsten Reuter[b] and Aijun Du [ID] *[a]

The deeper reduction of CO to multi-carbon-based fuels with higher energy densities and wider applicability has recently triggered extensive experimental and theoretical research. However, present-day catalysts for the generation of multi-carbon products (C_{2+}) suffer from ultra-high energy barrier for C–C bond formation and poor selectivity, which poses great challenges for practical application. Herein, we propose and evidence with first-principles calculations a novel catalyst for the conversion of CO into more value-added ethylene and ethanol under visible light, consisting of active Cu–B atomic pair decorated graphitic carbon nitride (Cu–B@g-C_3N_4). Our results show that the low coordinated Cu–B atomic pair anchored on g-C_3N_4 could effectively reduce the CO dimerization free energy barrier to a record value of 0.63 eV. This high catalytic performance stems from the moderate binding strength of the intermediates modulated by the asymmetric synergy of the atomically dispersed metal Cu and non-metal B that can break the linear scaling relationship of traditional transitional metal catalysts. Moreover, the low-coordinated Cu–B active site with synergistic d–p coupling can significantly suppress the parasitic hydrogen evolution reaction. Compared to pure g-C_3N_4, the Cu–B@g-C_3N_4 catalyst also becomes more optically active under visible and even infrared light. *Ab initio* molecular dynamics simulations suggest that the Cu–B@g-C_3N_4 catalyst possesses a high thermal stability. Considering that efficient catalysts for C_{2+} production are currently essentially limited to Cu-bimetallic systems, our work highlights a fully new concept towards the development of novel CO reduction catalysts based on synergistic coupling between metal Cu and non-metal atoms.

1. Introduction

The conversion of carbon dioxide into valuable carbon-based fuels by means of renewably generated electricity offers a green and sustainable way to address the existing energy and environment crisis brought by the burning of fossil fuels.[1] Although the reduction of CO_2 to carbon products, such as CO, HCOOH and CH_4, has been well investigated and established,[2] these simple single-carbon compounds are usually not the desirable products due to their relative lower value and energy density. Numerous efforts have therefore been made to explore means of deeper converting CO_2/CO to more value-added carbon products, in particular ethylene (CH_2CH_2) and ethanol (CH_3CH_2OH).[3] However, prohibitively high activation barriers

for C–C coupling and the undesired hydrogen evolution side reaction pose a grand and hitherto unmastered challenge.[4]

Copper is currently accepted as the best candidate for catalysing CO_2/CO to high-carbon alcohols and hydrocarbons, but the high overpotential (over 1.0 V) and low selectivity prevent its commercial application.[5,6] To improve the activity and selectivity, various Cu-based strategies have been pursued, such as changing the morphology,[7] tailoring different facets,[8] controlling the size,[9] pre-oxidizing the surface[10] and using nanosized copper.[11,12] Kanan *et al.* firstly proposed to construct oxide-derived nanocrystalline copper to reduce CO to ethanol and acetate, which can achieve a higher faradaic efficiency than that of polycrystalline Cu foil.[13] The improved performance was attributed to the grain boundaries in the oxide-derived Cu that can provide unique active sites for CO adsorption. Then Sargent *et al.* modified the copper catalyst by introducing hydroxide ions on or near the copper surface to lower the C–C coupling activation barriers.[14] Wang *et al.* reported that different Cu facets can modulate the energetics of initial C–C coupling and concluded that Cu(100) and stepped Cu(211) facets are more favourable to form C_2 products than prevalent Cu(111).[15] Even though these strategies could improve the catalytic performance to some extent, the observed faradaic efficiencies are still

[a]School of Chemistry, Physics and Mechanical Engineering, Queensland University of Technology, Garden Point Campus, Brisbane, QLD 4001, Australia. E-mail: aijun.du@qut.edu.au

[b]Chair for Theoretical Chemistry and Catalysis Research Center, Technical University of Munich, Lichtenbergstrasse 4, Garching 85747, Germany

This journal is © The Royal Society of Chemistry 2020

J. Mater. Chem. A, 2020, **8**, 599–606 | **599**

below 40%.[6,16–18] After extensive investigations, both experimental and theoretical results suggested that CO dimerization is the most energy consuming step for generating C_2 products.[19,20] Follow-up studies showed that the CO binding energies on the active sites need to be moderate to promote the C–C coupling reaction. On one hand, the CO should bind to the catalyst strong enough for further reduction, on the other hand, a too strong binding energy will result in very high activation barriers for the CO dimerization step.[21] Accordingly, recent works try to develop Cu-based bimetallic catalysts to tune this binding strength between the active sites and the adsorbate. Corresponding CuSn,[22] CuPd[23] and CuAg[24] bimetallic alloy catalysts have indeed shown improved catalytic performance for ethylene and ethanol production. In the alloyed metals the d-band of Cu moves to lower energies, which leads to a boost of the faradaic efficiencies toward C_2 products. Although tuning bimetallic systems is thus effective to modulate the binding strength, the achieved selectivity and activity for C_2 products remain far from the requirements. This is mainly attributed to the strong scaling relations between the adsorbates at extended transition metal catalyst surfaces, which severely limit the possibilities to significantly reduce the overpotentials.[25] Moreover, the comparatively large amount of noble metal required in these condensed bimetallic systems also prevents their future large-scale application.[26] Therefore, impending work is required to design novel catalysts which are capable of addressing these challenges.

According to the d-band model, the binding energies of the adsorbates are closely associated with the electron density of the metal d-states. If we introduce p-elements to hybridize with these states, the above mentioned scaling relations could possibly be broken. Recent experiments indeed demonstrated that a boron-modified Cu(111) surface could significantly improve the C_2 faradaic efficiency to 79%, while the boron doping could also enhance the stability of the catalyst during the electrochemical process.[27] Unfortunately, the free energy barrier for CO dimerization was still as high as 1.6 eV. In this situation, we recall that some works have shown that decreasing the size of the catalytic surface to the atomic level generally leads to unexpected, non-scalable catalytic properties.[28–30] The minimum catalytic surface is a single atom site, and corresponding single-atom catalysts have indeed attracted great interest following their experimental realization in 2011.[31] However, single-atom sites can only provide one active center to generate H_2,[32–34] O_2,[35,36] NH_3 (ref. 37 and 38) and at best catalyse simple single-carbon products.[39] To produce more value-added C_{2+} products, more than one active site is needed to adsorb the intermediates for C–C coupling.

Stimulated by the above studies, we here propose isolated Cu–B atomic pairs for this task. Porous optically active graphitic carbon nitride g-C_3N_4 can stably host such Cu–B atomic pairs within its structure.[40] Our first-principles calculations indeed suggest the resulting novel photocatalyst based on the concept of synergistic coupling between single copper and boron atoms to boost the conversion of CO to the C_2 products ethylene and ethanol. As expected, the asymmetric d–p orbital coupling in the Cu–B@g-C_3N_4 catalyst significantly reduces the CO

dimerization cost. Notably, the undesired competing hydrogen evolution reaction could be significantly suppressed during the CO reduction process. The high catalytic activity mainly attributes to the asymmetry synergy between metal Cu and non-metal B which overall leads to a moderate CO binding energy. Moreover, the light absorption of the Cu–B@g-C_3N_4 hybrid is greatly extended to the visible and infrared light region, and thus enables a solar-driven CO reduction. Additionally, preliminary *ab initio* molecular dynamics simulations performed at 1000 K suggest a rather high thermal stability of the Cu–B@g-C_3N_4 photocatalyst and thus a great potential for the experimental realization. The proposed synergy concept between single metallic and non-metallic asymmetric coupling could thus open a way to the rational design of novel catalysts for the reduction of CO to C_2 products under visible light.

2 Computational details

The Vienna *ab initio* simulation package (VASP) code was employed to perform the spin-polarized density-functional theory (DFT) calculations.[41,42] The projector-augmented wave (PAW) method was used to describe the ion–electron interactions.[43] Electronic exchange and correlation was treated at the generalized-gradient approximation (GGA) level as implemented in the Pardew–Burke–Ernzerhof (PBE) functional.[44,45] The DFT-D3 (ref. 46) approach was used in all calculations to address dispersive interactions. Solvation effects were considered by using the implicit solvation model implemented in VASPsol.[47,48] We used a periodic supercell containing a $2 \times 2 \times 1$ surface unit cell of one planar porous g-C_3N_4 sheet, *cf.* Fig. 1 below, with a vacuum layer of 20 Å decoupling the sheet from its periodic images. The kinetic energy cutoff was set to 500 eV, and the first Brillouin zone was sampled by a $3 \times 3 \times 1$ Monkhorst–Pack k-point grid. The convergence criteria for the force and energy difference were set to 0.005 eV Å^{-1} and 10^{-6} eV. The computational hydrogen electrode (CHE) model[4,49] was employed to include the electrode potential correction to the free energy of each state (details are in ESI†). Zero-point energies (ZPE), enthalpy and entropy contributions to the free energies were all considered and calculated as described in the ESI.† All structures were fully relaxed until residual forces fell below 0.005 eV Å^{-1}. Transition state searches were conducted with the climbing-image nudged elastic band (CI-NEB) method.[50] On the relaxed ground-state structures, optical adsorption spectra were calculated fixed-point with the Heyd–Scuseria–Ernzerhof (HSE) hybrid functional[51] and using a $6 \times 6 \times 1$ k-point grid. In addition, canonical *ab initio* molecular dynamics simulations (AIMDs) with a Nosé thermostat and integrating time with the Verlet algorithm at a time step of 2 fs were employed to investigate the thermodynamic stability of the catalyst.

3 Results and discussions

Stability of Cu–B@g-C_3N_4

The stability of the Cu–B@g-C_3N_4 catalyst is first examined by calculating the formation energies of single Cu and B atoms deposited on the g-C_3N_4 substrate. As shown in Fig. 1a, single
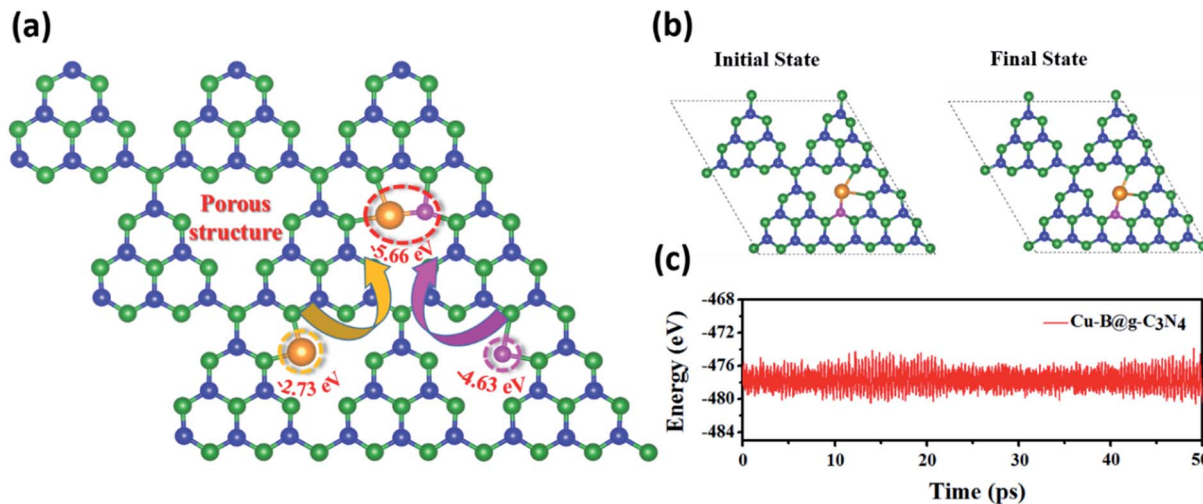
600 | *J. Mater. Chem. A*, 2020, **8**, 599–606

This journal is © The Royal Society of Chemistry 2020

Fig. 1 (a) Schematic design concept of Cu–B@g-C_3N_4 and the calculated formation energies for the single Cu, single B and Cu–B aromatic pair decorated g-C_3N_4. (b) The top view of the Cu–B aromatic pair anchored on a $2 \times 2 \times 1$ Cu–B@g-C_3N_4 supercell before and after the AIMD simulations. (c) The variations of energy with respected to the time for AIMD simulations of Cu–B@g-C_3N_4. The simulations are performed under 1000 K for 50 ps with a time step of 2 fs. Green, blue, bronze and pink balls stand for N, C, Cu and B atoms, respectively.

Cu and B atoms can be steadily anchored by the N-coordinating cavities after geometric optimization. The exothermic binding energies of Cu@g-C_3N_4 and B@g-C_3N_4 are −2.73 and −4.63 eV, which are in good agreement with previous experiments and calculations that equally obtained that single Cu or B can be stabilized on a g-C_3N_4 substrate.[52,53] For a co-deposited Cu and B atom pair on the g-C_3N_4 substrate, the calculated binding energy (−5.66 eV) becomes even more negative than the sum of the binding energies of an isolated Cu and B atom, *cf.* Fig. 1a. For comparison, the formation energy of (the experimentally realised)[40] Cu_2 and Fe_2 atomic pairs on g-C_3N_4 were also calculated and their binding energies are only −2.12 eV and −3.87 eV, respectively. Clearly, the adsorption of a Cu–B atomic pair on g-C_3N_4 is substantially more stable than that of Cu_2 and Fe_2 pairs. To further assess the thermodynamic stability of the formed Cu–B@g-C_3N_4 system, short-term canonical AIMD simulations were performed at an elevated temperature of 1000 K. As can be clearly seen in Fig. 1c, the energy is always oscillating around the equilibrium state and there is no significant structural destruction in the Cu–B@g-C_3N_4 nanohybrid (see Fig. 1b). It should be noted that the simulation temperature is at 1000 K which is higher than that of experimental temperature (900 K) for g-C_3N_4 fabrication.[54] The above evidences collectively indicate that asymmetric Cu–B pair can be steadily entrapped in the g-C_3N_4 substrate, demonstrating great potential for the experimental realization. In terms of recent experimental progress in the synthesis of the dispersed Fe_2 atomic pair on the g-C_3N_4 substrate by a "precursor-preselected" wet chemistry strategy,[40] the synthesis of the Cu–B@g-C_3N_4 catalyst appears highly feasible.

CO activation and dimerization

The activation of CO on the catalytically active sites is the first step for CO reduction. As presented in Fig. 2a and b, two CO molecules chemisorb on the Cu–B site pair with a combined binding energy of −2.19 eV. For comparison, the adsorption of two CO molecules on a Cu–Cu atomic pair is calculated as −3.52 eV, *i.e.* significantly stronger. This is also visible in the electron density difference plot in Fig. S1,† revealing an apparent electron transfer between the atomic pair and the CO molecules. For an optimum catalytic performance, the active sites should neither bind the *CO too weak (which will prevent further reduction) nor too strong (which will lead to high activation barriers) according to the Sabatier principle. Recent work by Zhou *et al.* suggests an optimum CO binding around −0.8 to −1.0 eV.[27] The average CO adsorption energy ($E_{avg} = E_{ad}(nCO)/n$) on the Cu–B@g-C_3N_4 catalyst is with −1.09 eV much closer to this optimal value than the one at a Cu–Cu atom pair (−1.76 eV). Moreover, the distance between a Cu–B pair is with 2.21 Å much shorter than the one between a Cu–Cu pair (2.79 Å), which should further facilitate the ensuing C–C coupling step. We also examined the N site adjacent to the Cu atom as potential active site to active CO molecules. However, the Co cannot bind to the N sites after the optimization, indicating catalytic inert of the N sites.

Most recent experiments suggested that the C–C coupling starts through a direct dimerization of two activated CO molecules to generate a *OCCO intermediate and then the *OCCO is hydrogenated to a *C_2O_2H intermediate.[15,27,55] The CO dimer had been observed in the reaction process which further confirmed the CO dimerization pathway.[56,57] Therefore, we take the CO–CO coupling pathway as the most likely C–C bond formation step and compare the C–C coupling reaction barrier of Cu–B@g-C_3N_4 to Cu–Cu@g-C_3N_4 and experimentally-available pure Cu(111) and boron-doped Cu(111) systems by computing the reaction free energies change along these C–C coupling paths at open circuit conditions, OCV (0 V *vs.* the reducible hydrogen electrode, RHE), and pH = 0 within the CHE model, as illustrated in Fig. 2. Clearly, the energy barriers for
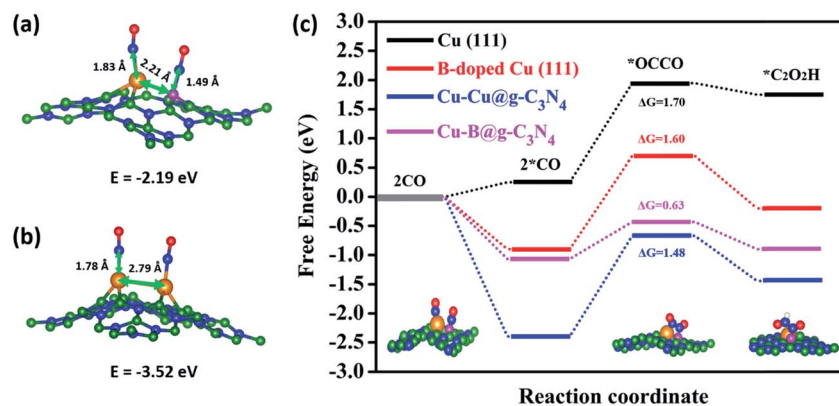
Fig. 2 Side view of the calculated geometric structures for CO adsorption at (a) Cu–B@g-C_3N_4 and (b) Cu–Cu@g-C_3N_4, (c) calculated free energy profiles of different active sites for C–C coupling at open circuit voltage (0 V *vs.* the reducible hydrogen electrode, RHE). The values for Cu(111) and B-doped Cu(111) are taken from ref. 27. Inserts show the corresponding structures of the reaction intermediates. Green, blue, bronze, pink, red and white balls represent N, C, Cu, B, O and H atoms, respectively.

C–C bond formation on experimentally reported pure Cu(111) and B-doped Cu(111) are both very high. However, with the size of the catalytic surface decreased to the atomic level, the catalytic activity has been significantly enhanced. Notably, the CO dimerization reaction energy on the asymmetric Cu–B@g-C_3N_4 catalyst is only one-third of the one at the experimental realised surface (1.60 eV).[27] We also explored some other possible reaction pathways (seeing Fig. S2 in the ESI†) and found the reaction free energies for the first hydrogenation step are as high as 1.13 eV and 2.90 eV, leading to very high overpotentials. In addition, we note that the extremely high free energy change to generate *CHO and *COH intermediates (the common intermediates for the production of methane and methanol) at Cu–B@g-C_3N_4 would also prevent the formation of C_1 products, potentially boosting the selective production of C_2 chemicals.

The overall CO reduction process on the Cu–B@g-C_3N_4 and Cu–Cu@g-C_3N_4 catalyst

After examining the plausible C–C coupling reaction route, we continue to investigate the subsequent conversion steps. For this we calculate the free energies for the possible reaction intermediates along these proton-coupled electron transfer steps again at OCV and pH = 0. We assessed solvation effects on these free energies within an implicit solvation model, but found the influence on the Gibbs free energy change (ΔG) for the first three reaction steps to be below <0.1 eV (Fig. S3†). For the remaining calculations, no solvation treatment was thus considered. In Fig. 3, the optimal pathways toward C_2 products including CH_2CH_2 and CH_3CH_2OH on the Cu–B@g-C_3N_4 and Cu–Cu@g-C_3N_4 catalysts are identified by comparing the lowest positive elementary free energy change for all the reaction steps. As can be seen in Fig. 3, the first five proton-coupled electron transfer steps follow the same reaction route, which begins with the hydrogenation of the adsorbed *OCCO intermediate to form *OCCHO after the formation of C–C bond – as was already included in Fig. 2 above. Then the *OCCHO intermediate is further hydrogenated to *OCCHOH, *HOCCHOH and

*HOCHCHOH with the smallest ΔG of 0.45 eV and 0.26 eV for the Cu–B and Cu–Cu atomic pair, respectively. When the next proton–electron pair attacks the *HOCHCHOH intermediate, the first H_2O molecule is generated with a *HOCHCH intermediate left on the active sites. Then, the reaction route starts to diverge on the two catalysts when the sixth proton–electron pair is transferred to the active sites. The *HOCHCH intermediate can be either hydrogenated to *HOCH$_2$CH or *CHCH (followed by the generation of another H_2O molecule). In case of the Cu–Cu@g-C_3N_4 catalyst, the ΔG are all endothermic for the remaining two reaction steps. In contrast, at the Cu–B@g-C_3N_4 catalyst, the *HOCHCH intermediate can be exothermically hydrogenated to *HOCH$_2$CH. With another two proton–electron pairs transferred to the intermediates, the two CO molecules are finally converted to CH_2CH_2 or CH_3CH_2OH. The rate-limiting step for the overall CO reduction is thus the initial C–C coupling step with a thermodynamic reaction free energy of 0.63 eV as discussed above, while the minimum thermodynamic rate-limiting step for the subsequent hydrogenation steps is below 0.5 V. Notably, the CH_3CH_2OH can be easily removed from the Cu–B@g-C_3N_4 surface after the last proton–electron pair was attached. Therefore, we anticipate a higher selectivity for the production of CH_3CH_2OH than C_2H_4. In order to compare the catalytic activity between the Cu–B@g-C_3N_4 catalyst and the experimentally realized boron-doped Cu(111) surface,[31] we replot the free energy profiles from ref. 31 in Fig. S4.† As mentioned above, the C–C coupling step on the boron-doped Cu(111) surface is as high as 1.60 eV, which is much higher than on the Cu–B@g-C_3N_4 catalyst (0.63 eV). Thus, we expect the atomically dispersed Cu–B@g-C_3N_4 catalyst to exhibit a dramatically increased performance to generate C_2 products.[19,20]

To obtain a better estimate for the key step, we finally conduct a transition state search to obtain the explicit activation barrier for this rate determining CO═CO coupling step. The calculated activation barrier for CO dimerization on Cu–B@g-C_3N_4 is as low as 0.99 eV (*i.e.* an additional kinetic barrier of 0.3 eV on top of the thermodynamic free energy barrier
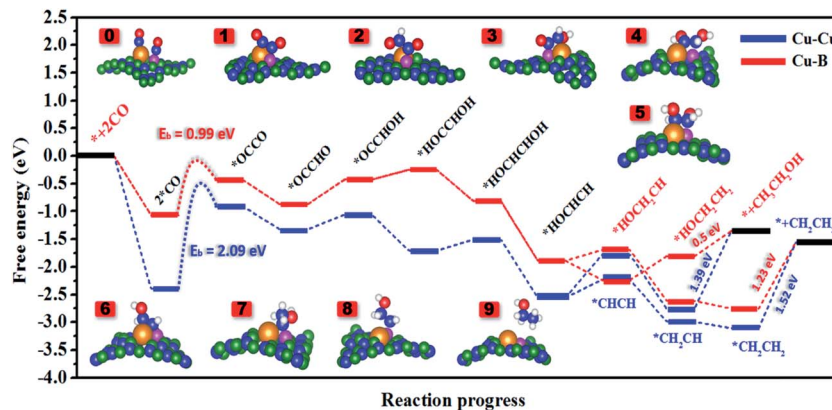
602 | *J. Mater. Chem. A*, 2020, **8**, 599–606

This journal is © The Royal Society of Chemistry 2020

Fig. 3 Free energy profile of CO reaction progress to CH_3CH_2OH and CH_2CH_2 on Cu–B@g-C_3N_4 (red line) and Cu–Cu@g-C_3N_4 (blue line) catalysts and the kinetic barrier (E_b) for the CO dimerization step. Inserts show the structures of the reaction intermediates for the optimal energy pathway to generate CH_3CH_2OH, where the red boxes with numbers represent the initial C–C coupling steps (0–1) and the eight subsequent proton-coupled electron transfer (2–9) steps. Green, blue, bronze, pink, red and white balls represent N, C, Cu, B, O and H atoms, respectively.

discussed above). This is much lower than the kinetic barrier on Cu–Cu@g-C_3N_4 (2.09 eV), Cu(211) (1.50 eV)[58] and is even superior to most of the reported catalysts for C_1 products (which are all over 1 eV).[59–61] As the kinetic barriers for proton transfer to adsorbates from solution are normally low enough to be surmountable at room temperature based on the pioneering studies,[62] we didn't calculate the reaction barriers for the hydrogenation steps. The above results collectively demonstrate that the Cu–B@g-C_3N_4 catalyst is a highly promising candidate to efficiently boost the conversion of CO_2/CO to C_2 products.

Competition between CORR and HER

Greatly impeding the faradaic efficiency, the hydrogen evolution reaction (HER) is the main undesired side reaction during the CORR. To assess this, we thus calculated the adsorption energy of a proton binding on the active site (*i.e.* the Volmer reaction step, $* + H^+ + e^- \rightarrow *H$). For the Cu–Cu atomic pair, the adsorption energy of *H is as high as −1.81 eV, which means the H^+ could be easily absorbed on the Cu–Cu active site and thus poison the CORR. In contrast, the adsorption energy of a proton on the Cu or B atom of Cu–B atomic pair is only −0.76 eV. This is less than the average CO adsorption energy (−1.09 eV) on the Cu–B atomic pair. This suggests the active sites to be preferentially occupied with *CO during the CORR. In addition, we also compare the reaction free energy profile of the HER on Cu–B@g-C_3N_4 and on the Cu(111) surface in Fig. S5.† The free energy for hydrogen evolution on Cu–B@g-C_3N_4 is much higher (0.53 eV *vs.* 0.19 eV on Cu(111)[52]), suggesting a significantly weaker hydrogen evolution ability. We therefore expect the synergy of the low-coordinated Cu–B atomic pair to also greatly improve the catalytic selectivity for the CORR.

Understanding the enhanced catalytic performance of the Cu–B@g-C_3N_4 catalyst

From our analysis to this point, it is clear that the moderate average binding energy of CO on the Cu–B@g-C_3N_4 catalyst

(∼−1.00 eV) is the key that drives an efficient CO=CO dimerization and generation of C_2 products. This is in contrast to the average CO binding energies on Cu–Cu (−1.76 eV) and B–B (−0.68 eV) active sites, these bindings are too strong or too weak, respectively. To further analyse this difference, we calculate the d- and p-band centers of Cu and B atoms in the Cu–Cu, Cu–B and B–B atom pairs. As shown in Fig. 4, the d-band center of Cu in Cu–Cu is at −1.57 eV below the Fermi level, which is much higher than for instance in the Cu(111) surface (∼3.40 eV), resulting in a much stronger binding strength as compared to the extended metal surface (−0.60 eV). For the B–B atom-pair, the p-band center is very deep (−2.29 eV), concomitantly leading to a CO binding strength (−0.68 eV) quite weak. Now, within the Cu–B pair, the d-band center of the Cu atom shifts to lower energies (from −1.57 to −1.68 eV), while the p-band center of B atom shifts to higher energies (from −2.29 to −1.70 eV). As a result, the binding strength of one CO on Cu site of Cu–B pair become weaker (−1.04 eV *vs.* −1.76 eV), while the binding strength of one CO on B site of Cu–B pair get stronger (−1.36 eV *vs.* −0.68 eV). This leads to the very moderate average CO binding energy (−1.09 eV) on Cu–B pair. As apparent from Fig. 4, these beneficial shifts result from a weakened hybridization of Cu and a strengthened hybridization of B in the Cu–B pair as compared to the Cu–Cu and B–B pair, respectively. This breaks the linear scaling relationship controlling adsorption at the traditional transition metal catalyst and thus significantly improves the thermochemistry and kinetics of CO_2/CO reduction to C_2 products.

Solar-driven CO reduction

g-C_3N_4 is not only an excellent substrate but also a well-known semiconductor which can provide photogenerated electrons under light irradiation.[63] However, the pristine g-C_3N_4 exhibits limited visible light absorption, which greatly hinders its practical utilization for solar energy conversion.[64,65] As shown in Fig. 5 and consistent with previous studies,[60,63–66] we find that pristine g-C_3N_4 can only harvest light in the ultraviolet region.
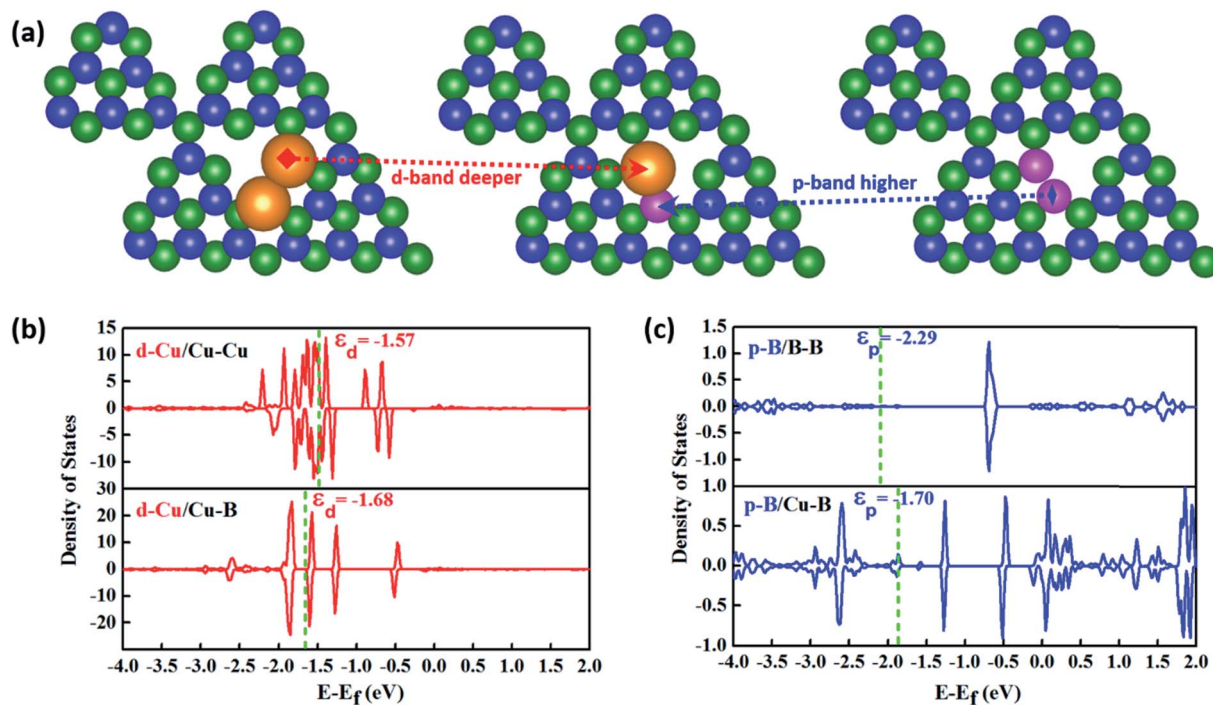
This journal is © The Royal Society of Chemistry 2020

J. Mater. Chem. A, 2020, **8**, 599–606 | **603**

Fig. 4 (a) Structural models for Cu–Cu, Cu–B and B–B anchored on g-C_3N_4. The d-band centers of Cu in (b) Cu–Cu@g-C_3N_4 and Cu–B@g-C_3N_4, and p-band centers of B in (c) B–B@g-C_3N_4 and Cu–B@g-C_3N_4. Green, blue, bronze and pink balls stand for the N, C, Cu and B atoms, respectively.
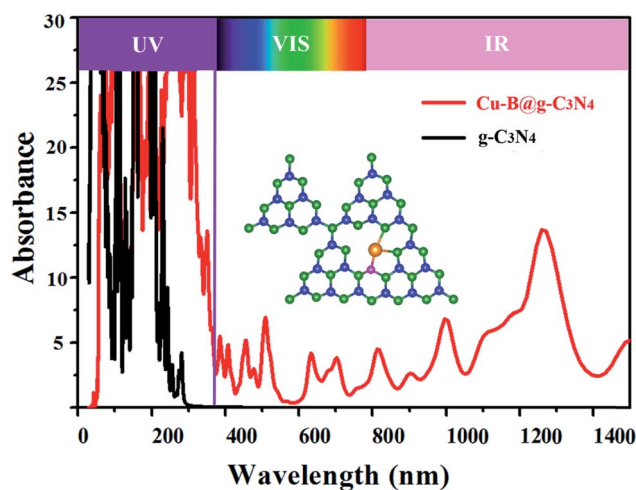

Fig. 5 Calculated optical adsorption spectrum for Cu–B atom pair decorated g-C_3N_4 and pristine g-C_3N_4. The insert shows again the structure of the Cu–B@g-C_3N_4 catalyst.

Excitingly, the Cu–B atom-pair decorated g-C_3N_4 (Cu–B@gC_3N_4) catalyst exhibits a significantly extended light absorption spectrum to the visible (VIS) and even infrared (IR) light regions. Moreover, the band gap of the pristine g-C_3N_4 is narrowed by Cu–B doping, leading to more efficiency of charge trapping, transfer and separation that will all benefit the CO reduction under light irradiation. Possibly, these could even enable a solar driven conversion of CO_2/CO to C_2 products, a most promising topic of future research and experimental verification.

4. Conclusions

In summary, we for the first time report a novel asymmetric Cu–B@g-C_3N_4 catalyst based on a fully new concept on the synergistic coupling between metal (d-orbital) and non-metal (p-orbital). The Cu–B@g-C_3N_4 catalyst can boost the conversion of CO to high density more value-added C_2 products (ethylene and ethanol) with high activity and selectivity. The Cu–B@g-C_3N_4 possesses an ultralow reaction energy (only 0.63 eV) for the CO dimerization, which is nearly one-third of that for the boron-doped Cu(111) catalyst (1.60 eV). Most importantly, the most uphill hydrogenation step for generation CH_3CH_2OH is only 0.53 eV and the product could be easily desorbed from the catalytic surface. The electronic structure analysis reveals that the asymmetric synergy between the single Cu and B atom altered the d-band center of Cu and p-band center of B to achieve a moderate CO binding strength. Additionally, the optical absorption of the Cu–B@g-C_3N_4 can be extended the visible and infrared light region, which enable the more efficient utilization of solar energy. It is also important to note that the Cu–B@g-C_3N_4 hybrid catalyst possesses much lower formation energy than those of single Cu or B decorated g-C_3N_4 and exhibits high thermal stability under 1000 K. Our results not only highlight a novel hybrid nanocatalyst for the reduction of CO to C_2 products, but offers a fully new concept on the use of asymmetric metal and non-metal coupling to modulate the linear scaling relationship of traditional transitional metal catalysts and the deign principle is capable to apply to other novel electrochemical or photochemical catalysts.

604 | *J. Mater. Chem. A*, 2020, **8**, 599–606

This journal is © The Royal Society of Chemistry 2020

Conflicts of interest

There are no conflicts to declare.

Acknowledgements

References

1 M. Asadi, K. Kim, C. Liu, A. V. Addepalli, P. Abbasi, P. Yasaei, P. Phillips, A. Behranginia, J. M. Cerrato and R. Haasch, *Science*, 2016, **353**, 467–470.

2 J. Gu, C.-S. Hsu, L. Bai, H. M. Chen and X. Hu, *Science*, 2019, **364**, 1091–1094.

3 T. T. Hoang, S. Verma, S. Ma, T. T. Fister, J. Timoshenko, A. I. Frenkel, P. J. Kenis and A. A. Gewirth, *J. Am. Chem. Soc.*, 2018, **140**, 5791–5797.

4 A. A. Peterson, F. Abild-Pedersen, F. Studt, J. Rossmeisl and J. K. Nørskov, *Energy Environ. Sci.*, 2010, **3**, 1311–1315.

5 M. B. Gawande, A. Goswami, F.-X. Felpin, T. Asefa, X. Huang, R. Silva, X. Zou, R. Zboril and R. S. Varma, *Chem. Rev.*, 2016, **116**, 3722–3811.

6 K. P. Kuhl, E. R. Cave, D. N. Abram and T. F. Jaramillo, *Energy Environ. Sci.*, 2012, **5**, 7050–7059.

7 P. De Luna, R. Quintero-Bermudez, C.-T. Dinh, M. B. Ross, O. S. Bushuyev, P. Todorović, T. Regier, S. O. Kelley, P. Yang and E. H. Sargent, *Nat. Catal.*, 2018, **1**, 103.

8 T. Cheng, H. Xiao and W. A. Goddard, *Proc. Natl. Acad. Sci. U. S. A.*, 2017, 201612106.

9 D. Kim, C. S. Kley, Y. Li and P. Yang, *Proc. Natl. Acad. Sci. U. S. A.*, 2017, 201711493.

10 H. Xiao, W. A. Goddard, T. Cheng and Y. Liu, *Proc. Natl. Acad. Sci. U. S. A.*, 2017, 201702405.

11 W. Zhu, Y.-J. Zhang, H. Zhang, H. Lv, Q. Li, R. Michalsky, A. A. Peterson and S. Sun, *J. Am. Chem. Soc.*, 2014, **136**, 16132–16135.

12 S. Sen, D. Liu and G. T. R. Palmore, *ACS Catal.*, 2014, **4**, 3091–3095.

13 C. W. Li, J. Ciston and M. W. Kanan, *Nature*, 2014, **508**, 504.

14 C.-T. Dinh, T. Burdyny, M. G. Kibria, A. Seifitokaldani, C. M. Gabardo, F. P. G. de Arquer, A. Kiani, J. P. Edwards, P. D. Luna, O. S. Bushuyev, C. Zou, R. Quintero-Bermudez, Y. Pang, D. Sinton and E. H. Sargent, *Science*, 2018, **360**, 783–787.

15 K. Jiang, R. B. Sandberg, A. J. Akey, X. Liu, D. C. Bell, J. K. Nørskov, K. Chan and H. Wang, *Nat. Catal.*, 2018, **1**, 111.

16 D. Gao, I. T. McCrum, S. Deo, Y.-W. Choi, F. Scholten, W. Wan, J. G. Chen, M. J. Janik and B. Roldan Cuenya, *ACS Catal.*, 2018, **8**, 10012–10020.

17 C. W. Li and M. W. Kanan, *J. Am. Chem. Soc.*, 2012, **134**, 7231–7234.

18 R. Reske, H. Mistry, F. Behafarid, B. Roldan Cuenya and P. Strasser, *J. Am. Chem. Soc.*, 2014, **136**, 6978–6986.

19 H. Xiao, T. Cheng, W. A. Goddard III and R. Sundararaman, *J. Am. Chem. Soc.*, 2016, **138**, 483–486.

20 K. D. Yang, C. W. Lee, K. Jin, S. W. Im and K. T. Nam, *J. Phys. Chem. Lett.*, 2017, **8**, 538–545.

21 X. Liu, J. Xiao, H. Peng, X. Hong, K. Chan and J. K. Nørskov, *Nat. Commun.*, 2017, **8**, 15438.

22 X. Zheng, Y. Ji, J. Tang, J. Wang, B. Liu, H.-G. Steinrück, K. Lim, Y. Li, M. F. Toney and K. Chan, *Nat. Catal.*, 2018, 1.

23 S. Ma, M. Sadakiyo, M. Heima, R. Luo, R. T. Haasch, J. I. Gold, M. Yamauchi and P. J. Kenis, *J. Am. Chem. Soc.*, 2016, **139**, 47–50.

24 E. L. Clark, C. Hahn, T. F. Jaramillo and A. T. Bell, *J. Am. Chem. Soc.*, 2017, **139**, 15848–15857.

25 Y. Li and Q. Sun, *Adv. Energy Mater.*, 2016, **6**, 1600463.

26 A. J. Martín, G. O. Larrazábal and J. Pérez-Ramírez, *Green Chem.*, 2015, **17**, 5114–5130.

27 Y. Zhou, F. Che, M. Liu, C. Zou, Z. Liang, P. De Luna, H. Yuan, J. Li, Z. Wang and H. Xie, *Nat. Chem.*, 2018, **10**, 974.

28 W. E. Kaden, T. Wu, W. A. Kunkel and S. L. Anderson, *Science*, 2009, **326**, 826–829.

29 A. Corma, P. Concepción, M. Boronat, M. J. Sabater, J. Navas, M. J. Yacaman, E. Larios, A. Posadas, M. A. López-Quintela and D. Buceta, *Nat. Chem.*, 2013, **5**, 775.

30 M. Nesselberger, M. Roefzaad, R. F. Hamou, P. U. Biedermann, F. F. Schweinberger, S. Kunz, K. Schloegl, G. K. Wiberg, S. Ashton and U. Heiz, *Nat. Mater.*, 2013, **12**, 919.

31 B. Qiao, A. Wang, X. Yang, L. F. Allard, Z. Jiang, Y. Cui, J. Liu, J. Li and T. Zhang, *Nat. Chem.*, 2011, **3**, 634.

32 Y. Xue, B. Huang, Y. Yi, Y. Guo, Z. Zuo, Y. Li, Z. Jia, H. Liu and Y. Li, *Nat. Commun.*, 2018, **9**, 1460.

33 T. He, C. Zhang and A. Du, *Chem. Eng. Sci.*, 2019, **194**, 58–63.

34 T. He, G. Gao, L. Kou, G. Will and A. Du, *J. Catal.*, 2017, **354**, 231–235.

35 H. Fei, J. Dong, Y. Feng, C. S. Allen, C. Wan, B. Volosskiy, M. Li, Z. Zhao, Y. Wang and H. Sun, *Nat. Catal.*, 2018, **1**, 63.

36 T. He, S. K. Matta, G. Will and A. Du, *Small Methods*, 2019, 1800419.

37 H. Li, J. Shang, Z. Ai and L. Zhang, *J. Am. Chem. Soc.*, 2015, **137**, 6393–6399.

38 T. He, S. K. Matta and A. Du, *Phys. Chem. Chem. Phys.*, 2019, **21**, 1546–1551.

39 S. Back, J. Lim, N.-Y. Kim, Y.-H. Kim and Y. Jung, *Chem. Sci.*, 2017, **8**, 1090–1096.

40 S. Tian, Q. Fu, W. Chen, Q. Feng, Z. Chen, J. Zhang, W.-C. Cheong, R. Yu, L. Gu and J. Dong, *Nat. Commun.*, 2018, **9**, 2353.

41 G. Kresse and J. Furthmüller, *Comput. Mater. Sci.*, 1996, **6**, 15–50.

This journal is © The Royal Society of Chemistry 2020

J. Mater. Chem. A, 2020, **8**, 599–606 | **605**

42 G. Kresse and J. Hafner, *Phys. Rev. B: Condens. Matter Mater. Phys.*, 1993, **47**, 558.

43 P. E. Blöchl, *Phys. Rev. B: Condens. Matter Mater. Phys.*, 1994, **50**, 17953.

44 J. P. Perdew, J. A. Chevary, S. H. Vosko, K. A. Jackson, M. R. Pederson, D. J. Singh and C. Fiolhais, *Phys. Rev. B: Condens. Matter Mater. Phys.*, 1992, **46**, 6671.

45 J. P. Perdew and Y. Wang, *Phys. Rev. B: Condens. Matter Mater. Phys.*, 1992, **45**, 13244.

46 S. Grimme, *J. Comput. Chem.*, 2006, **27**, 1787–1799.

47 K. Mathew and R. G. Hennig, 2016, arXiv preprint arXiv:1601.03346.

48 K. Mathew, R. Sundararaman, K. Letchworth-Weaver, T. Arias and R. G. Hennig, *J. Chem. Phys.*, 2014, **140**, 084106.

49 J. K. Nørskov, J. Rossmeisl, A. Logadottir, L. Lindqvist, J. R. Kitchin, T. Bligaard and H. Jonsson, *J. Phys. Chem. B*, 2004, **108**, 17886–17892.

50 G. Henkelman, B. P. Uberuaga and H. Jónsson, *J. Chem. Phys.*, 2000, **113**, 9901–9904.

51 J. Heyd, G. E. Scuseria and M. Ernzerhof, *J. Chem. Phys.*, 2003, **118**, 8207–8215.

52 Y. Jiao, Y. Zheng, P. Chen, M. Jaroniec and S.-Z. Qiao, *J. Am. Chem. Soc.*, 2017, **139**, 18093–18100.

53 C. Ling, X. Niu, Q. Li, A. Du and J. Wang, *J. Am. Chem. Soc.*, 2018, **140**, 14161–14168.

54 S. Yan, Z. Li and Z. Zou, *Langmuir*, 2009, **25**, 10397–10401.

55 X. Liu, P. Schlexer, J. Xiao, Y. Ji, L. Wang, R. B. Sandberg, M. Tang, K. S. Brown, H. Peng and S. Ringe, *Nat. Commun.*, 2019, **10**, 32.

56 F. Calle-Vallejo and M. T. Koper, *Angew. Chem., Int. Ed.*, 2013, **125**, 7423–7426.

57 E. Pérez-Gallent, M. C. Figueiredo, F. Calle-Vallejo and M. T. Koper, *Angew. Chem., Int. Ed.*, 2017, **129**, 3675–3678.

58 J. H. Montoya, A. A. Peterson and J. K. Nørskov, *ChemCatChem*, 2013, **5**, 737–742.

59 C. Liu, B. Yang, E. Tyo, S. Seifert, J. DeBartolo, B. von Issendorff, P. Zapol, S. Vajda and L. A. Curtiss, *J. Am. Chem. Soc.*, 2015, **137**, 8676–8679.

60 G. Gao, Y. Jiao, E. R. Waclawik and A. Du, *J. Am. Chem. Soc.*, 2016, **138**, 6292–6297.

61 Y. Yang, J. Evans, J. A. Rodriguez, M. G. White and P. Liu, *Phys. Chem. Chem. Phys.*, 2010, **12**, 9909–9917.

62 C. Shi, K. Chan, J. S. Yoo and J. K. Nørskov, *Org. Process Res. Dev.*, 2016, **20**, 1424–1430.

63 X. Wang, K. Maeda, A. Thomas, K. Takanabe, G. Xin, J. M. Carlsson, K. Domen and M. Antonietti, *Nat. Mater.*, 2009, **8**, 76.

64 S. Cao, J. Low, J. Yu and M. Jaroniec, *Adv. Mater.*, 2015, **27**, 2150–2176.

65 Y. Wang, X. Wang and M. Antonietti, *Angew. Chem., Int. Ed.*, 2012, **51**, 68–89.

66 T. He, C. Zhang, L. Zhang and A. Du, *Nano Res.*, 2019, **12**, 1817–1823.

606 | *J. Mater. Chem. A*, 2020, **8**, 599–606

This journal is © The Royal Society of Chemistry 2020